Controlled autoignition of hydrogen in a direct-injection optical engine

Pavlos G. Aleiferis *, Martino F. Rosati

Department of Mechanical Engineering, University College London, UK

ARTICLE INFO

ABSTRACT

Research into novel internal combustion engines requires consideration of the diversity in future fuels in an attempt to reduce drastically CO_2 emissions from vehicles and promote energy sustainability. Hydrogen has been proposed as a possible fuel for future internal combustion engines and can be produced from renewable sources. Hydrogen's wide flammability range allows higher engine efficiency than conventional fuels with both reduced toxic emissions and no CO_2 gases. Most previous work on hydrogen engines has focused on spark-ignition operation. The current paper presents results from an optical study of controlled autoignition (or homogeneous charge compression ignition) of hydrogen in an engine of latest spark-ignition pentroof combustion chamber geometry with direct injection of hydrogen (100 bar). This was achieved by a combination of inlet air preheating in the range 200–400 °C and residual gas recirculated internally by negative valve overlap. Hydrogen fuelling was set to various values of equivalence ratio, typically in the range ϕ = 0.40–0.63. Crank-angle resolved flame chemiluminescence images were acquired for a series of consecutive cycles at 1000 RPM in order to calculate in-cylinder rates of flame expansion and motion. Planar Laser Induced Fluorescence (LIF) of OH was also applied to record more detailed features of the autoignition pattern. Single and double (i.e. 'split' per cycle) hydrogen injection strategies were employed in order to identify the effect of mixture preparation on autoignition's timing and spatial development. An attempt was also made to review relevant in-cylinder phenomena from the limited literature on hydrogen-fuelled spark-ignition optical engines and make comparisons were appropriate.

© 2012 The Combustion Institute. Published by Elsevier Inc. Open access under CC BY license.

1. Introduction

1.1. Background

1.1.1. Hydrogen properties

The main advantage of burning hydrogen in internal combustion engines is its lack of carbon content, leading locally to no exhaust emissions of particulate matter, unburned hydro-carbons, CO and CO_2. A general review of the research done on hydrogen as a fuel for automotive applications up to the mid 90s has been given by Norbeck et al. [1]. More recent reviews have been published by White et al. [2], Verhelst et al. [3,4] and Verhelst and Wallner [5]. Some of hydrogen's properties, particularly relevant to in-cylinder mixture formation and combustion, are summarised in Table 1 in comparison to those of gasoline and methane [6–8]. Hydrogen has very low density and, although its heating value on a mass basis is very high in comparison to other fuels (120 MJ/kg for hydrogen, 43.5 MJ/kg for gasoline), on a volume

basis this is the lowest (10.2 MJ/m^3 for hydrogen, 216.4 MJ/m^3 for gasoline). NO_X emissions from stoichiometric combustion of hydrogen are comparable to those from engines fuelled by gasoline or common gaseous fuels. However, it is possible to burn hydrogen in much leaner/cooler flames than common carbon-based fuels; this leads to quite low NO_X emissions, especially for ϕ < 0.5; Exhaust Gas Recirculation (EGR) can also be used to control the combustion duration and NO_X emissions from SI hydrogen engines [9–13]. Hydrogen's minimum ignition energy is about one order of magnitude less than that of common fuels; it also has a small quenching distance which means that it can autoignite easily and its flame can get past a nearly closed intake valve more readily and backfire into the intake manifold. Hydrogen is also prone to engine knocking. The reason for such 'uncontrolled' autoignition issues is dependent on load. One could argue that a fuel with such a high Research Octane Number (RON $\geq$ 130) should not show tendency to knock but hydrogen does not fit well into the normal definitions of octane number. It has a very high RON but very low Motor Octane Number (MON) [14]. MON is a better measure of how the fuel behaves under load because MON testing uses a similar test engine to that used in RON testing, but with a preheated fuel mixture, a higher engine speed and variable ignition timing to further stress the fuel's knock resistance. Typically, the MON

* Corresponding author. Address: University College London, Department of Mechanical Engineering, Torrington Place, London WC1E 7JE, UK. Fax: +44 (0)20 73880180.
E-mail address: p.aleiferis@ucl.ac.uk (P.G. Aleiferis).

Nomenclature

λ	air excess ratio	ETU	Engine Timing Unit
ϕ	equivalence ratio	EVC	Exhaust Valve Closure
		EVO	Exhaust Valve Open
Abbreviations		HCCI	Homogeneous Charge Compression Ignition
AIT	After Ignition Timing	LIF	Laser Induced Fluorescence
ATDC	After intake Top Dead Centre	IMEP	Indicated Mean Effective Pressure
BDC	Bottom Dead Centre	IVC	Intake Valve Closure
BTDC	Before Compression TDC	IVO	Intake Valve Open
CA	Crank Angle	PFI	Port Fuel Injection
CAI	Controlled AutoIgnition	PIV	Particle Image Velocimetry
DI	Direct Injection	RPM	Revolutions Per Minute
DISI	Direct Injection Spark Ignition	SI	Spark Ignition
EGR	Exhaust Gas Recirculation	SOI	Start of Injection

of a modern gasoline is about 8–10 points lower than the RON; hydrogen, with a much lower MON than RON, has a relatively low knock resistance in practice.

1.1.2. Hydrogen mixture formation in engines

Particularly due to pre-ignition/backfire and NO_X-related problems, injection systems and mixture preparation strategies for hydrogen engines have attracted a lot of attention. However, no commercial injectors have been fully developed yet specifically for the life-cycle of a hydrogen engine because much larger volumes of fuel must be injected per stroke due to the very low density of hydrogen; hydrogen's low lubricity also leads to severe durability problems for injectors that have been designed for common fuels [15]. Nevertheless, commercial Port Fuel Injection (PFI) systems for common gaseous fuels can be adopted for engine operation with hydrogen for research and/or demonstration purposes that do not entail long running engine times. However, with PFI, even if one uses strategies to prevent backfire by retarding the injection (such that the end of injection is timed to occur just prior to intake valve closure), the in-cylinder charge has ~20% lower calorific value at stoichiometric conditions than a gasoline–air mixture (due to air displacement from the large volume of injected hydrogen) that leads to a large power deficit and the requirement to supercharge the engine [16,17]. Hence, adoption of hydrogen DI systems seems to offer certain potential because hydrogen can be injected when the intake valves have already closed, therefore, backfire is not an issue and no air is displaced during injection.

Although various technical problems of hydrogen injection in engines have been tackled and solved in an empirical manner, little work has been published on optical diagnostics of hydrogen combustion in modern engine designs. Laser Induced Fluorescence (LIF) techniques, based on acetone or other fuel dopants, have re-

cently been developed particularly for the study of mixture formation in hydrogen engines with high pressure DI systems [18–22] and some of these have been combined with Particle Image Velocimetry (PIV) to provide insights into the interactions between the jets of hydrogen's DI and the in-cylinder flowfield [23,24]. Specifically, such studies have demonstrated that with hydrogen DI timings after Intake Valve Closure (IVC) there is strong interaction between hydrogen's jets and in-cylinder air flow, resulting in significant changes to the in-cylinder charge motion at the end of compression in comparison to non-fuelled in-cylinder flow fields. Furthermore, with such injection strategies, hydrogen can end up concentrated mostly close to the cylinder walls, leading to strong fuel stratification and inhomogeneities in the in-cylinder charge prior to ignition along with a high degree of turbulence intensity in the mixing regions, despite hydrogen's high diffusivity.

1.1.3. Hydrogen Controlled AutoIgnition (CAI) or Homogeneous Charge Compression Ignition (HCCI)

SI gasoline and Compression Ignition (CI) Diesel engines have recently been accompanied by CAI or HCCI engines. CAI/HCCI engines may be considered as hybrids of SI and CI engines because these use premixed charge as SI engines do, but the charge is forced to autoignite by compression as in CI engines. Autoignition occurs simultaneously at multiple points across the cylinder, resulting in very fast combustion and enabling all the heat to be released within a short time space. The combination of fast heat release and the use of a lean charge, gives close to constant volume combustion with low peak gas temperatures leading to reduced heat transfer losses through the cylinder. The main benefits of HCCI are very low NO_X emissions and overall improvements in fuel economy/efficiency [25]. For HCCI engines the use of high compression ratios has been deemed essential. Conventional SI engine

Table 1
Properties of hydrogen in relation to those of gasoline and methane.

Parameter	Hydrogen	Gasoline	Methane
Density (kg/m³)	0.09 (0 °C) 71 (−253 °C)	5.1 (vapour) 730–780	0.72 (0 °C) 423 (−162 °C)
Stoichiometry (kg_{Air}/kg_{Fuel})	34.3	14.7	17.2
Lower heating value (MJ/kg)	120	43.5	50
Lower heating value at ϕ = 1 (MJ/kg)	3.40	2.83	2.72
Boiling temperature (°C)	−253	25–215	−162
Ignition limits (Vol.%, ϕ)	4–75, 0.1–6.67	1.0–7.6, 0.71–2.5	5.3–15, 0.48–1.43
Minimum ignition energy at ϕ = 1 (mJ)	0.02	0.24	0.29
Autoignition temperature (°C)	585	350	540
Quenching distance (mm)	0.64	2.0	2.03
Kinematic viscosity (m²/s)	110×10^{-6}	1.18×10^{-6}	17.2×10^{-6}
Thermal conductivity (W/m K)	182.0×10^{-3}	11.2×10^{-3}	34.0×10^{-3}
Diffusion coefficient in air (m²/s)	6.1×10^{-5}	0.5×10^{-5}	1.6×10^{-5}

designs are typically limited to a compression ratio of approximately 11:1 (the latter mainly for DISI engines that benefit from the effects of increased charge cooling from liquid fuel injection), therefore quite sophisticated systems are required to enable HCCI on current engine geometries. Large amounts of residual-gas recirculation and/or air-preheating are essential to achieve HCCI [26–29] and use of fully variable valve timing systems with fully flexible valve timing strategies are needed to promote various levels of non-cooled internal EGR and also effectively induce variable compression ratios over a range of engine operating conditions.

Although HCCI engines have been reported to be very fuel flexible from the outset [30] and significant HCCI literature already exists on a variety of fuels [31], there is still very little knowledge on the use of hydrogen as the only fuel in HCCI engines. The autoignition temperature and diffusivity of hydrogen are both higher than those of gasoline or mixtures of heptane/iso-octane in air, implying a very different mixing and autoignition mechanism. Stenlååns et al. [32] studied hydrogen HCCI in on one of the six cylinder of a single-cylinder thermal CI engine of large capacity (1.6 l) at high compression ratios (typically 15:1–20:1) using external mixture preparation and air preheating. They found that intake temperatures of the order 80–160 °C were needed for successful operation in the range $\phi = 0.167$–0.25 for 800–1600 RPM; NO$_X$ emissions were negligible. More recent work published by Gomes Antunes et al. [33] presented hydrogen HCCI measurements from a thermal engine of 0.825 l equipped with a PFI system within a similar operation range to that identified by Stenlååns et al. [32]. They reported that by hydrogen fuelling the engine achieved a fuel efficiency of 43% compared to 28% in Diesel-fuelled mode; a 20% reduction in NO$_X$ was also observed. Caton and Pruitt [34] used experiments in a single-cylinder Cooperative Fuels Research (CFR) Diesel engine and a single-zone model with chemical reaction kinetics to show that hydrogen HCCI exhibited combustion efficiencies of 90–95%. Emissions of NO$_X$ were typically below 1 ppm and at least two orders of magnitude lower than a comparable Diesel cycle.

Laser Induced Fluorescence (LIF) studies in HCCI engines fuelled by common carbon-based fuels have revealed that HCHO and OH species are present within the 'cool' flame period and subsequent 'hot' combustion, respectively [35–37]. The absence of carbon atoms, and thus HCHO, from the in-cylinder mixture of a hydrogen HCCI engine means that a totally different mechanism of autoignition is in operation and that OH distribution can be very different from that of hydrocarbon fuels. However, there are currently no studies in the literature that have discussed explicitly hydrogen HCCI in optical research engines using OH LIF and flame chemiluminescence imaging. This is one of the gaps in the literature that the current paper wishes to fill; specific objectives are summarised in the following section.

1.2. Present contribution

Recent work by the current authors focused on analysis of in-cylinder combustion phenomena from an optical engine fuelled with hydrogen PFI and DI and presented rates of in-cylinder flame growth and motion under SI operation [38]. The present work aims to focus solely on hydrogen HCCI and discuss data from that same optical engine fuelled with hydrogen DI, aiming to characterise the mechanism of hydrogen's controlled autoignition by:

- High-speed imaging of flame chemiluminescence.
- Imaging of hydrogen's flame structure by planar laser induced fluorescence of OH.
- Quantifying in-cylinder autoignition behaviour by measures of flame expansion speed and motion.
- Examining the effect of injection strategy on the nature of autoignition and combustion development.

The study has been conducted in pentroof combustion chamber geometry (typical of latest SI engines) and, to the authors' knowledge, this is the first optical engine running on hydrogen HCCI that is being characterised by the aforementioned combination of techniques and analysis in the literature. Therefore, it is believed to contribute towards a database of hydrogen combustion in engines which is essential for developing our knowledge of the underlying fundamental mechanisms. Such data are also essential for modellers because simulation of complex in-cylinder combustion phenomena from an engine designer's perspective can be very challenging. Furthermore, one of the secondary – but still important – objectives of the current study was to provide links between in-cylinder hydrogen HCCI and optical data collected from hydrogen SI operation, as well as data from in-cylinder hydrogen mixture formation studies in the recent literature. Comparison with traditional modes of HCCI combustion of carbon-based fuels was also deemed essential. This attempt provides a general framework for analysis of phenomena from various engines and fuels.

2. Experimental apparatus and procedure

2.1. Optical engine

The engine used in this study was a single-cylinder research engine designed and built at University College London (UCL). The bore of the engine was 89 mm and the stroke was 79 mm; the compression ratio was 7.5. Geometrical properties of the engine, along with other specifications are summarised in Table 2. A hollow 'Bowditch' piston allowed for a 45° stationary mirror to be fitted inside the block in order to gain optical access to the combustion chamber through a quartz piston crown. A vacuum pump was connected to the crankcase to draw oil-laden gas out and reduce smearing of the mirror and the piston crown. The engine design also accommodated a pentroof window and side full stroke window for optical access through the liner. However, it was only the piston optical crown and the small pentroof window, that were retained for the current study due to uncertainties involved with the thermal stressing of the engine when run with hydrogen fuelling. Engine control was achieved by using shaft encoders, with a resolution of 1800 pulses per revolution, fixed to the engine's camshafts and crankshaft, as well as an AVL 427 Engine Timing Unit (ETU). The encoder also fed a Top Dead Centre (TDC) reference to the ETU. The engine's head and block were heated via an independent water circulation system and heat exchanger. The engine speed was set to 1000 RPM. The engine temperature was set to 85 °C to represent typical warm running engine conditions. The throttle was set to wide-open position for 1.0 bar intake manifold pressure.

2.2. Fuel supply systems and injectors

The engine accommodated a flexible fuelling system, capable of both PFI and DI of liquid and gaseous fuels. Three injectors were fitted on the engine, two on the intake ports allowing for

Table 2
Engine specifications.

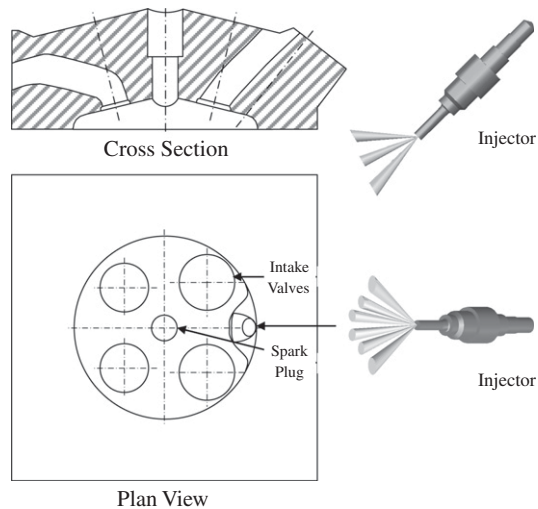|	
Engine type	4-Stroke, single-cylinder optical
Engine head	4-Valve pentroof (Prototype V8)
Piston shape	Flat
Bore/stroke (mm)	89/79
Optical bore (mm)	66
Displacement (cm^3)	498
Injection system	PFI, DI
Valve timings (° CA ATDC)	IVO 36, IVC 266, EVO 482, EVC 712

Fig. 1. Combustion chamber geometry and orientation of injector with nominal spray pattern.

simultaneous injection of liquid and gaseous fuels and one in-cylinder for DI engine operation. For the purposes of the current work, hydrogen DI operation was of primary interest. Selection of a hydrogen injector for DI fuelling was not trivial. The engine head had been originally designed to operate with a side gasoline pressure–swirl atomizer at 45° inclination located between the intake valves and one of the requirements of the DI system was to allow flexibility for use with both liquids and gases. A multi-hole gasoline injector was selected to replace the pressure swirl atomiser. The injector nozzle had a 6-hole arrangement that consisted of two groups of three asymmetric holes originally designed for a spray-guided DI gasoline combustion system with vertically mounted injector in close-spacing arrangement with the spark plug. This was a cost-effective choice able to cope with the high flow-rate requirements needed for hydrogen. However, it must be pointed out that it was only due to the short running periods involved with optical engine operation that it was possible to adopt safely such a solution (hydrogen's low lubricity would not allow the injector to live long). The position of the injector and its nominal spray pattern with respect to the combustion chamber are

shown in Fig. 1. Due to the asymmetry of the nozzle-hole pattern, after several tests of the engine's operation stability, an orientation with the two sets of plumes pointing upwards towards the pentroof was finally adopted as shown in Fig. 1.

Hydrogen was supplied by pressurised bottles to the DI hydrogen system. The fuel supply system also comprised a back-flash arrestor, a micrometric in-line filter and a mass-flow controller (Bronkhorst F-203AC); the injection pressure was set to 100 bar by a pressure regulator; this was the highest permitted by the mass-flow controller. The latter was calibrated by the manufacturer for hydrogen operation and connected via a serial cable to a PC in order to monitor and control the fuel flow to the injector in real time. To measure the air-to-fuel ratio, provision was made in the exhaust manifold for a heated exhaust gas oxygen (UEGO) sensor.

2.3. Air preheating and internal EGR

For HCCI operation the engine was fitted with an air pre-heating system of 2.3 kW that could control the intake air temperature in the range 50–400 °C. A necessary step to achieve hydrogen HCCI in this engine was to adapt the valve timings and trap hot residual gases in order to further increase in-cylinder temperature and retain chemical species. The strategy employed was of retarded Intake Valve Closing (IVC) time and advanced Exhaust Valve Opening (EVO) time which led to a small recompression at intake TDC. This was done in two stages. The first stage enabled a reduced valve overlap in comparison to that of the nominal design and was used to enable HCCI of heptane and mixtures of heptane and hydrogen [39]. The second stage in Fig. 2 aimed at decreasing even more the valve overlap by further retardation of the IVC (hence IVO as cam profiles were kept the same) and further advancement of the EVC (hence EVO), finally switching to 44° CA negative valve overlap for all measurements of the current study. Table 2 summarises the operating conditions adopted. It should be noted that in this paper 0° CA corresponds to Intake Top Dead Centre (TDC) and crank angle will be mainly presented with respect to that as ° CA After intake TDC (ATDC). The residual gas fraction in the engine was calculated by modelling the engine's operation using geometrical and valve timing data via the detailed methodology offered by the Lotus engine simulation software [40] and was found to be 22% for Stage 1 and 42% for Stage 2.
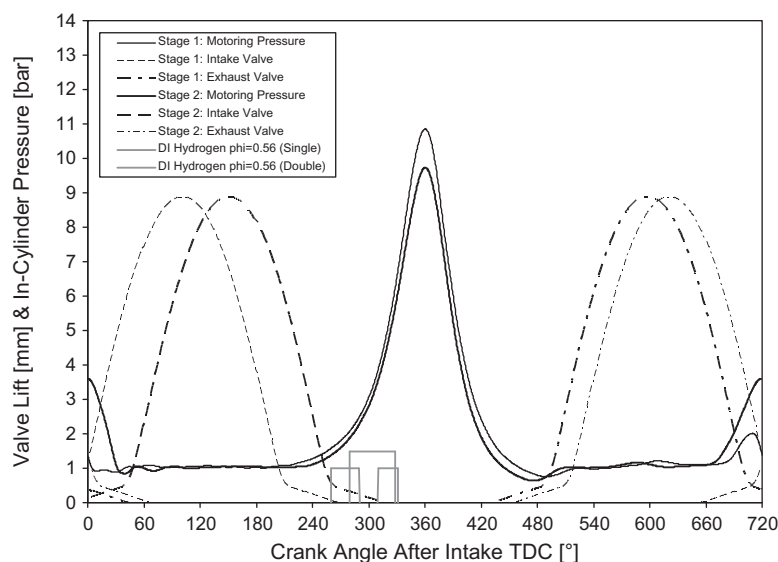

Fig. 2. Valve cam profiles, motoring pressures and injection strategies.

2.4. Injection strategies

Injection strategies with different timings of Start of Injection (SOI) were used. Primarily, a single-injection strategy per cycle with SOI at 280° CA ATDC was adopted. This was dictated by several constraints: it could not be advanced as it was bound by IVC timing and it would also cool excessively the charge, but it could not be retarded either because this would not allow enough mixing time before ignition. For $\phi = 0.56$ the single injection per cycle lasted 8 ms, *i.e.* 48° CA at 1000 RPM. Considering the closed-valve DI strategy approach, and based on in-cylinder hydrogen mixture formation studies in the literature [20–24], it can be said that the mixture cannot really be fully premixed at autoignition. This will be discussed in more detail in the results section and highlights the use of the term 'CAI' for this paper in favour of 'HCCI'. In order to further investigate this aspect of mixture formation, it was decided to enable a second injection strategy by splitting the injection event into two sequential smaller pulses per cycle, whilst keeping the total amount of fuel delivered per cycle the same. The strategy consisted of a first pulse with SOI = 260° CA ATDC and a second pulse with SOI = 310° CA ATDC. The first pulse of the double injection strategy had a duration of 5.0 ms, *i.e.* 30° CA, whilst the second lasted for 3.5 ms, *i.e.* 21° CA. The injection pulses of the single and double injection strategies have been included in Fig. 2 on the same graph of valve timings and motoring pressures to aid the reader in his understanding.

2.5. Pressure measurements and analysis

The in-cylinder pressure measurements for the present study were conducted with a water-cooled piezo-electric pressure transducer (Kistler 6041A) connected to a Kistler 5011B10 charge amplifier; absolute pressure referencing was done via the mean intake manifold pressure. The in-cylinder pressure signals were digitised on a cycle-to-cycle basis with a 12-bit analogue-to-digital converter (National Instruments PCI-MIO-16E-4) within LabVIEW at a resolution of 0.4° CA at 1000 RPM. The uncertainty due to electrical interference was a maximum of 0.05% of the full scale value for the in-cylinder pressure and 1% of full scale value for the intake plenum and barrel pressures, corresponding to an uncertainty of ±5.0 mbar and ±10 mbar, respectively. Thermodynamic analysis was done on the pressure traces using methods published in [38,39]. The errors involved in acquiring and processing were carefully considered. The effects of numerical integration associated with calculating indicated work can be minimised provided the crank angle resolution is smaller than 1° CA; according to [41] a ±0.5° CA uncertainty in the phasing of TDC gives ±2.5% uncertainty in IMEP. Errors will also arise from the effects of signal noise, accurate definition of con-rod length and the correct phasing of TDC with pressure. In the current arrangement the accuracy of the con-rod length was accurate to below 0.01% and the position of TDC was accurate to within less than ±0.1° CA such that errors due to the experimental setup were considered negligible. A representative number of cycles for analysis was identified on the basis of COV_{IMEP}. Cyclic variability in IMEP was typically quite small (typically less than 2%) and achieved steady-state values at ~100 cycles max depending on conditions, hence 100 consecutive cycles were elected for analysis at all conditions. This included imaging as discussed in the next paragraphs.

2.6. High-speed chemiluminescence imaging

A high-speed CMOS camera (Photron APX-RS) was used for crank-angle resolved chemiluminescence imaging. Specifically, the camera was employed at a frame rate of 6 kHz, corresponding respectively to 1° CA between frames at 1000 RPM. This was done

for image sizes of 640 × 480 pixels, giving a resolution of 160 µm per pixel. No filters were used in order to capture broadband light emission. However, a detailed spectroscopic study was undertaken in parallel and this will be reported in a future publication. Synchronisation of various control triggers for ignition, injection and camera was achieved using the optical encoder on the camshaft as engine clock connected to the AVL Engine Timing Unit. Once image acquisition was complete, images were downloaded from the camera via IEEE 1394 FireWire to a PC system for image storage as 8-bit Tagged Image File Format (TIFF) files in 256 greyscales.

In order to obtain quantitative information from the combustion images flame areas were obtained on a cycle-by-cycle basis via thresholding/binarisation of each flame image to define the 'projected' in-cylinder enflamed area by summing up the pixels that had intensity higher than a threshold. Great care was exercised to define an appropriate circular region of interest on the flame images in order to isolate the flame only chemiluminescence without picking up any light from reflections at the boundaries of the circular window of the piston crown. The methodology was checked 'on-line' for each processed flame to ensure that visually the flame areas were being faithfully reproduced for the whole period of flame growth. Mean flame growth curves were plotted for all fuels in terms of an 'equivalent radius' calculated from the flame areas of all individual cycles based on the area of a circle equal to the total flame area measured from each image. Flame speeds were inferred from flame radii by using a finite-difference approach and plotted both in time and against flame size.

The geometric centroid of area for each flame was identified in x and y image co-ordinates and calculated for the duration of flame growth. The centroid co-ordinates were used to plot the ensemble-averaged flame centroid motion path. This was considered essential after observation of the autoignition pattern, as will be presented in the results section. Some bias in the real centroid location might be introduced from chemiluminescence masking effects once the flame has grown out of the field of view but major flame motion trends between different conditions are still valid on a relative basis. The rate of change of that displacement, *i.e.* the flame centroid speed, was also calculated for comparison with the flame growth speed and data from the literature on other fuels.

Uncertainties in the calculated ensemble averaged flame area were estimated by considering a single binarised flame. The area calculated for this flame was compared to the area of the same flame with an extra pixel added to the equivalent flame radius. This was considered to represent an uncertainty linked to the spatial resolution of the imaging arrangement. Second, the change in the binarised area of a flame due a change in the threshold value was also computed. For small flame areas of 2–3 mm equivalent radius, these uncertainties were found to be 9% and 0.2–0.4% per threshold unit of the nominal equivalent flame radius, respectively, the latter reflecting clearly the low sensitivity of the threshold value to the flame area calculation in the early stages of combustion. For larger flames of ~15 mm equivalent radius, considering a wider window of uncertainty due to higher flame luminosity of ±5 pixels the uncertainties were found to be 1–2% of the equivalent flame radius.

2.7. Oh laser induced fluorescence imaging

The pump laser was a Continuum Surelite III Nd:YAG. In order to obtain light of 532 nm the second harmonic was used. The beam was then steered into a Sirah Cobra Stretch dye laser. It was chosen to excite rotational lines of the transition $A^2\Sigma^+$ ($v' = 1$) ← $X^2\Pi$ ($v'' = 0$) which were deemed those capable of strong signals, hence the excitation wavelength required from the dye laser had to be in

the range from 279.00 to 291.00 nm. Rhodamine 6G dye was employed; it has high photostability, high quantum yield (0.95) and it lasing range has close proximity to its absorption maximum (approximately 530 nm). The light coming from the excited dye, or fundamental wavelength at 566 nm, crossed a frequency doubler again, resulting in a maximum output at $\sim$283 nm, which is optimal when seeking rotational lines in the range cited earlier. The lines in the range from 284 to 281 nm were the ones which yielded the strongest signals and the rotational line at 282.90 nm was finally selected after fine tuning. Energy of the order 400 mJ per pulse was necessary from the Nd-YAG to obtain $\sim$25 mJ max per pulse from the dye laser. The mirrors adopted to drive the beam exiting the dye laser beam were Techspec Nd:YAG Laser 266 nm, which had near 100% reflection at the wavelengths adopted. The sheet maker employed was a LaVision cylindrical $f/20$ lens with embedded focusing mechanism. The shape resulting from the arrangement was a 0.5×60 mm laser sheet, entering the engine 1 mm above the combustion deck.

The camera employed for OH LIF was a Princeton Instruments Intensified Charge Couple Device (ICCD), PI-MAX camera with an array size of 512×512 pixels. The camera was fitted with a P43 photocatode for maximum efficiency in the UV. 100 ns gating was employed as this was compatible with the typical timings involved with an internal combustion engine. A Nikon 105 mm $f/4.5$ UV lens was used to collect light coming from the combustion chamber via the UV enhanced mirror located in the hollow piston extension. The optical parts were realised in UV polished fused silica for both piston and side pentroof window. In order to resourcefully isolate the fluorescence signal from broadband chemiluminescence and block scattered light, a combination of Schott UG11 and Schott WG 305 filters was employed. The WG 305 filter was used to block all the light with wavelengths shorter than 305 nm, including all the scattering generated by the laser light at 293 nm. The UG 11 filter was employed to block most of the visible spectrum, allowing band-pass from 245 to 410 nm (peak at 340 nm). The pair of filters transmitted $\sim$56% of the incident radiation in the band between 305 and 320 nm. In order to control the camera and Laser triggers with nanosecond precision, a Stanford Signal Generator was employed to finely adjust the pulses coming from the ETU. Figure 3 shows the optical arrangement for OH LIF imaging. The intensifier was set to $\sim$85% of its maximum gain to eliminate increased levels of digital noise at maximum nominal output.

3. Results and discussion

3.1. In-cylinder pressure analysis

Figure 4 shows in-cylinder pressure traces for ϕ = 0.50–0.63 and with intake temperature of 200–400 °C. ϕ = 0.63 was set as the rich limit for this study in order to avoid damage to the optical components of the engine due to the combination of high temperatures and peak in-cylinder pressures involved. From a lean limit point of view, it was possible to sustain hydrogen HCCI combustion typically down to ϕ = 0.33, but intake temperatures in excess of 400 °C were needed, that were again overstressing the engine's optical components, hence no major runs were done at this test point.

In Fig. 4 for ϕ = 0.63 the start of heat release occurred earlier than for ϕ = 0.50–0.56, at $\sim$330° CA ATDC and peak pressure occurred later, namely at $\sim$375° CA, which was 10° CA later than that for ϕ = 0.50 and ϕ = 0.56. The effect of intake air temperature in the range 200–400 °C was not very strong for ϕ = 0.63 as shown in Fig. 4; a 200 °C raise in intake temperature was just enough to produce an advance in the phasing of the start of heat release by $\sim$3° CA and $\sim$3 bar increase in peak in-cylinder pressure, but with very small difference in the phasing of peak pressure ($\sim$1° CA). When fuelling was decreased to ϕ = 0.50, autoignition was not easily sustainable with intake temperatures lower than 200 °C and, although 300 °C allowed stable HCCI, increasing the temperature from 300 °C to 400 °C did not show much stronger effects than those observed for ϕ = 0.63. For comparison, a 20 °C increase in intake air temperature for heptane HCCI with ϕ = 0.72, advanced the autoignition angle by 10° CA and increased the peak pressure by about 3 bar in the same engine [39], broadly similar to what has been observed in other optical research engines with similar compression ratio at similar running conditions [26–29].

Literature on experimental hydrogen HCCI is scarce, e.g., see [32–34] where tests have been carried out at high compression ratios (15:1–20:1) primarily in Diesel engine geometries with no optical access. Some of the trends observed in the current optical engine can be considered consistent with what could be expected by extrapolation from those few earlier studies. For example, Stenlååss et al. [32] showed that for ϕ = 0.22, when engine speed was decreased from 1600 RPM to 800 RPM, an increase in intake air temperature of 20 °C was needed to sustain HCCI. This is typically opposite to what has been observed for heptane HCCI where it has been easier to achieve controlled autoignition at 600 RPM with
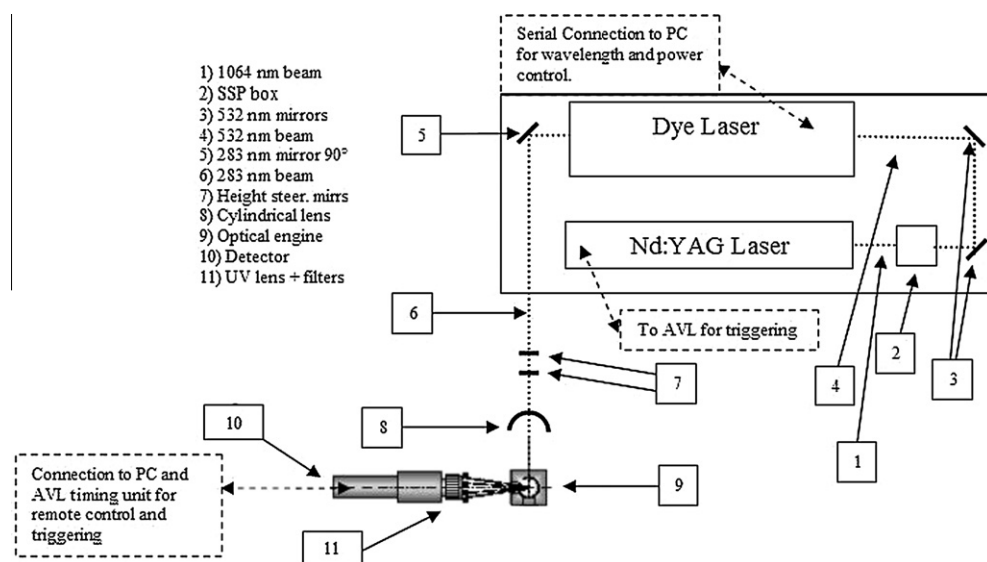

1) 1064 nm beam
2) SSP box
3) 532 nm mirrors
4) 532 nm beam
5) 283 nm mirror 90°
6) 283 nm beam
7) Height steer. mirrs
8) Cylindrical lens
9) Optical engine
10) Detector
11) UV lens + filters

Serial Connection to PC for wavelength and power control.

Dye Laser

Nd:YAG Laser

To AVL for triggering

Connection to PC and AVL timing unit for remote control and triggering
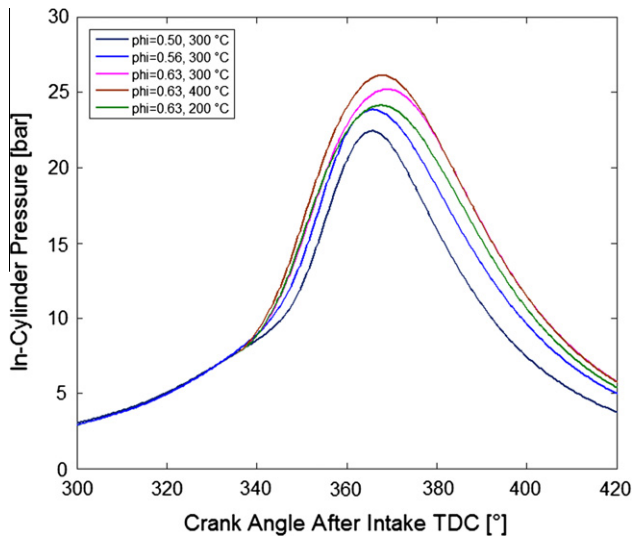
Fig. 3. Setup for OH LIF.

Fig. 4. In-cylinder pressure traces.

lower intake temperatures than at 1500 RPM. However, it seems consistent with the need for intake temperatures in excess of 200 °C to enable hydrogen HCCI at 1000 RPM with equivalence ratio lower than $\phi = 0.63$ in the engine of the current study that had much lower compression ratio than the engines of [32–34]. More to the point, when the compression ratio was decreased from 20:1 to 15:1 in [32], an increase in intake temperature from 80 °C to 150 °C was required to enable hydrogen HCCI. On such a trend line and by extrapolation it seems again consistent that temperatures of up to 400 °C were needed for successful HCCI, especially when considering again the lower compression ratio used in the current study. The effect of increasing intake temperature in the study of Stenlåås et al. [32] was much stronger than that of the current study; at $\phi = 0.22$, 1200 RPM and 17:1 compression ratio, an increase of 10 °C (from 107 °C to 117 °C), led to an increase in peak in-cylinder pressure from 45 to 60 bar and the ignition angle was advanced by 10° CA (from 12° CA ATDC to 2° CA ATDC).

3.2. Flame chemiluminescence imaging

3.2.1. General characteristics

The change in intake air temperature by 200 °C had a small influence on the timing of the first sign of flame chemiluminescence in the images, consistent with the observations made from the pressure traces in the previous section. Figure 5 shows typical intra-cycle images of hydrogen autoignition with equivalence ratio in the range $\phi = 0.50$–0.63 and intake temperature set to 300 °C. The intake valves and injector nozzle are located at the top in the images and the exhaust valves at the bottom; crank-angle timings are given sequentially with reference to the timing shown at the top. The mechanism of hydrogen autoignition was very different to in-cylinder phenomena that have been observed in past work for either heptane or blends of heptane and iso-octane. Specifically, for $\phi = 0.50$ with single-injection strategy shown in the first column of Fig. 5, autoignition started on the right-hand-side of the combustion chamber, between the intake and exhaust valves close to the wall, and followed a clockwise swirling path motion during development until it filled up the cylinder bore. This happened at the same location with limited spatial variability on a cycle-by-cycle basis and followed broadly the same pattern of development too; the cycle-to-cycle variability in the timing of autoignition was also quite small, typically in the range ±2° CA. The end of

the single injection event per cycle was ~10° CA before the start of autoignition (Fig. 2), hence the 'swirling motion' of autoignition might have been a result of the strong effect of momentum exchange between the hydrogen DI jets and the in-cylinder air. For hydrogen SI operation at low load (0.5 bar intake pressure), flames have been observed to expand relatively symmetrically with respect to the spark plug location [38]. At high load (1.0 bar intake pressure) however, SI flames have shown some large-scale distortion upon propagation similar to that observed for the HCCI flames of the current study, typically swirling in clockwise direction after they had a reached a size about half that of the optical bore upon 'symmetric' initial expansion from the spark-plug location [38,39]. However, valve timings were different for SI operation in those earlier studies and the residual gas fraction was about half that imposed by the valve timings of HCCI operation. In order to study this feature of combustion development in more detail, SI operation was enabled with the valve timings of HCCI under wide-open-throttle conditions, but without enabling air preheating to avoid engine knocking effects. High-speed images revealed that on this setting SI flames followed consistently a preferential direction of motion/expansion from the central spark-plug location towards the exhaust side of the cylinder first and then rapidly moved back towards the intake side of the engine following circumferential patterns on either side. This resembled a motion as if two counter-rotating flow vortices were recirculating on either sides of the bore over the left and right set of intake and exhaust valves. This flame behaviour for SI operation is shown in the fourth column of Fig. 5 (AIT stands for After Ignition Timing) for direct comparison with that of the HCCI flames. The 'swirling' nature of HCCI combustion in clockwise direction might be a result of similar in-cylinder flow field and mixture concentration to those of SI, but with autoignition starting on the right-hand side of the bore between the intake and exhaust valves (instead of at the centre of the bore), and expanding with high speed towards the left-hand side of the combustion chamber (i.e. in opposite direction to the large-scale recirculating flow pattern on the right-hand-side), any flow field effects were not initially as clear as with SI combustion. However, once the flame had crossed over to the lower left quadrant of the bore, it is plausible that the left-hand-side flow pattern that operated in the same direction to that of the flame on this side now supported the flame's principal direction of motion and forced it to exhibit a 'swirling' effect. Critically, the overall effect may be due to a balance of flow and preferential fuel stratification effects; this will be discussed in some detail slightly later in this paper.

When the equivalence ratio was set to $\phi = 0.63$, autoignition started again on the right-hand-side of the combustion chamber between the intake and exhaust valve, but not in close proximity to the cylinder's walls. The first site of autoignition had shifted towards the centre of the bore, laying typically half-way between the centre of the bore and the outer boundary of the optical bore, as shown in the second column of Fig. 5. This behaviour was again consistent on a cycle-by-cycle basis. Initial expansion was generally of 'circular' shape but once the flame size had reached about half that of the optical bore it expanded towards the left-hand-side area of the combustion chamber, it started to exhibit large-scale distortion akin to the swirling motion observed for $\phi = 0.50$ flames too.

Finally, the third column of Fig. 5 presents a typical cycle of autoignition with double (i.e. 'split') injection event per cycle. The equivalence ratio was set to $\phi = 0.50$ with 300 °C intake temperature for direct comparison to the observations made with single-injection strategy at the same conditions in first column of the same figure. With this setting, no 'swirling' combustion pattern was observed; autoignition started always close to the centre of the bore and developed towards the walls, filling up the bore gradually in a fairly symmetrical fashion. This could be explained
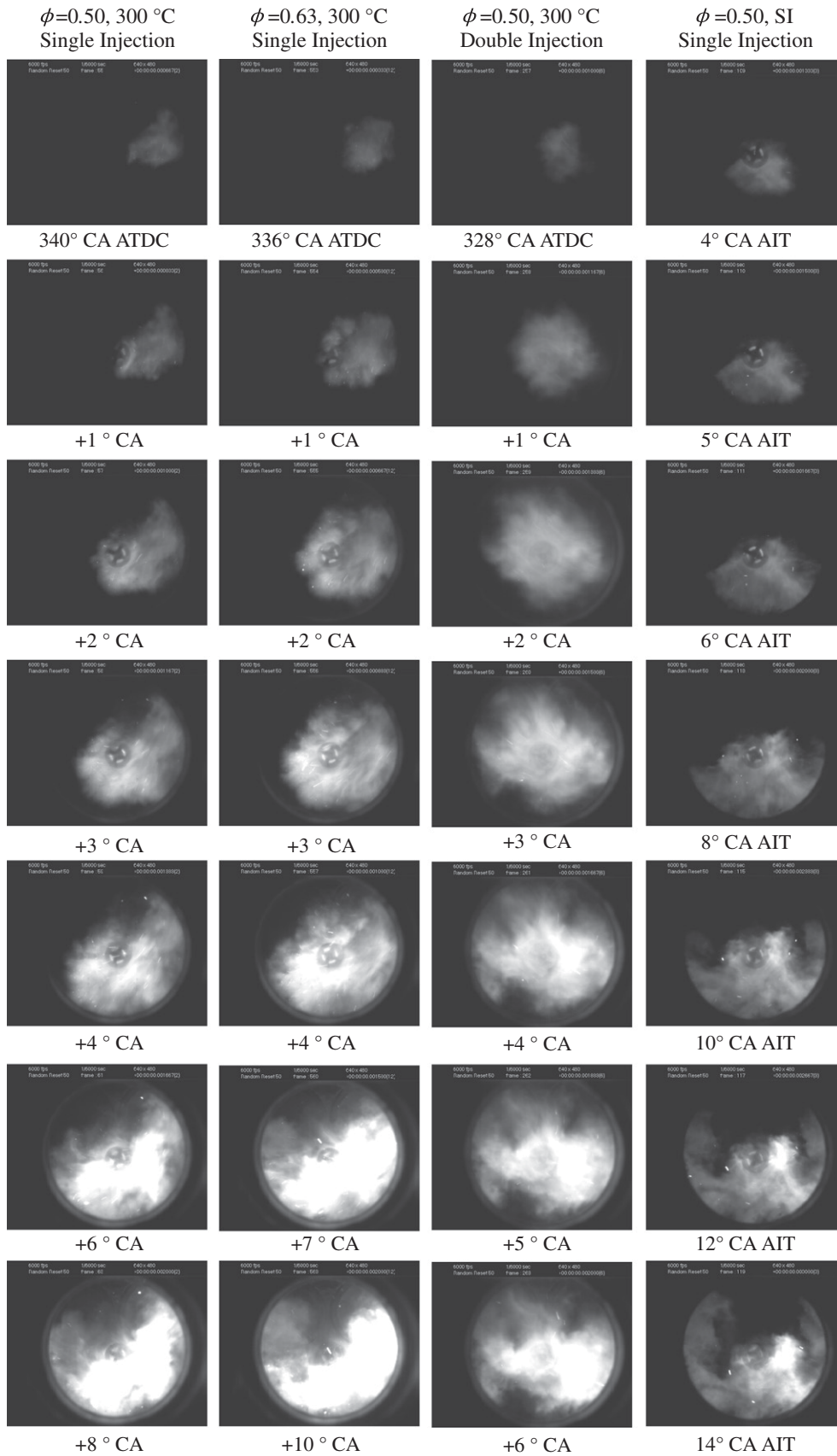
ϕ=0.50, 300 °C Single Injection	ϕ=0.63, 300 °C Single Injection	ϕ=0.50, 300 °C Double Injection	ϕ=0.50, SI Single Injection
340° CA ATDC	336° CA ATDC	328° CA ATDC	4° CA AIT
+1 ° CA	+1 ° CA	+1 ° CA	5° CA AIT
+2 ° CA	+2 ° CA	+2 ° CA	6° CA AIT
+3 ° CA	+3 ° CA	+3 ° CA	8° CA AIT
+4 ° CA	+4 ° CA	+4 ° CA	10° CA AIT
+6 ° CA	+7 ° CA	+5 ° CA	12° CA AIT
+8 ° CA	+10 ° CA	+6 ° CA	14° CA AIT

Fig. 5. Flame images: ϕ = 0.50–0.63 (intake valves at the top, exhaust valves at the bottom).

by a weaker effect of the two short hydrogen injection pulses on the in-cylinder air flow motion; however, it is also plausible that the double-injection strategy promoted faster mixing of the injected hydrogen with the in-cylinder air, leading to lower gradients of stratification and hence to absence of ultra lean areas of fuel concentration. Autoignition with double-injection started earlier than with single injection, typically at about 30–32° CA Before TDC (BTDC), *i.e.* about 10–12° CA earlier than with the single-injection, and about 5° CA before the end of the second pulse of injection, hence, autoignition occurred during the final stage of the hydrogen jetting process. However, despite the earlier start, location of peak pressure was only advanced by ∼6° CA from that of single injection at the same running conditions, exhibiting also similar peak value to that of single injection (∼22 bar). It is worth noting that double injection allowed typically autoignition with leaner values of equivalence ratio and at lower intake temperatures; for example, at $\phi = 0.45$ with intake temperature in the range 200–250 °C controlled autoignition was possible with double injection, but very difficult to enable and sustain with single injection. Therefore, it is believed that by selecting different types of multiple-injection strategies, it could be possible to control and phase better the start of autoignition to match different engine running conditions.

Considering that the objectives of the current work were focussed on studying combustion dynamics, investigations of mixture formation and in-cylinder flow were not undertaken; this decision was made because such work has been done by other authors in hydrogen engines of similar geometry, hence a review of those could provide a general picture of the flow/mixing phenomena inside the engine of the current study and links with the current findings. Specifically, work done by White [20,21] with LIF imaging of acetone-doped hydrogen in a DISI engine with a side multi-hole injector concluded that for pre-IVC injection, or for SOI coincident with IVC, a near-homogeneous mixture distribution existed irrespective of injection pressure (up to 100 bar tested). However, SOI after IVC led to hydrogen wall impingement with fuel accumulation close to the cylinder walls on one side of the combustion chamber and much leaner mixture in the remainder of the cylinder, especially close to the centre of the bore. In further LIF research using acetone-doped hydrogen, Salazar and Kaiser [22,23] studied various hydrogen injector nozzle geometries and locations (multi-hole and single-hole, side and central) with 100 bar fuel pressure and showed that injection after IVC yielded inhomogeneous mixtures with similar features for all injectors. Specifically, with SOI at 280° CA ATDC (*i.e.* same to that of the current study), convection of the fuel pattern was much more three-dimensional than observed for earlier SOI, with hydrogen rolling over the piston top and being deflected sideways along the cylinder liner, leading to hydrogen being mostly concentrated again near the cylinder walls. High and low tumble ratios showed minor differences in the overall flow patterns during and shortly after injection, presumably due to the large momentum of hydrogen's injection that was relatively insensitive to the momentum of the existing in-cylinder air flow.

Kaiser and White [24] combined LIF with PIV to study hydrogen mixture formation from a side multi-hole injector and found that for post-IVC SOI, the hydrogen injection event changed significantly the in-cylinder flow field when compared to the non-fuelled flow field. The portion of the optical bore with mean velocities in the range 5–10 m/s had increased substantially, with a strong mean flow motion coming back from the exhaust side towards the injector on the intake side. Moreover, the overlay of PIV and LIF data showed spatial correlation and it was concluded that the stable counter-flow field had resulted from interactions between the hydrogen jets and the combustion chamber's walls that redirected the hydrogen flow back down and towards the injector;

after the end of injection, the back-flow appeared to break up into a counter-rotating vortex pair, promoting mixing.

Comparing those findings with the flame images of Fig. 5, it may be hypothesised that a similar motion was induced by interactions between the hydrogen injection jets and the cylinder's walls in the engine of the current study; *i.e.* fuel instead of rolling over the piston and getting evenly distributed within the cylinder, it was diverted towards the cylinder walls and its momentum was redirected onto circumferential paths along the liner. Therefore, it may be suggested that local mixture distribution dictated the location of the onset of autoignition near the engine's walls and then subsequent flame development was affected by the in-cylinder flow motion and mixture distribution that had resulted from hydrogen-jet/wall interactions. The injection strategies that allowed HCCI operation throughout the current set of experiments appeared to be consistently close to the intermediate injection strategy employed by [20,21,24–26] for SI hydrogen operation with matching fuel injection pressure, which may suggest that this could be a reasonable trade-off when deliberately seeking a certain degree of mixture stratification for both SI and HCCI operation. SI experiments in the current engine [38] have strengthened this conclusion too.

3.2.2. Flame motion

The motion of the autoignited combustion pattern was analysed quantitatively from the high-speed images at varying operating conditions. The co-ordinates of the flame's geometrical centroid of area were extracted and plotted to show how the flames were displaced from the geometrical centre of the bore throughout the main stages of combustion, 2–25° CA after the start of autoignition. Figure 6 shows those results; the general 'swirling' flow trend for all mixtures prepared by the single-injection strategy is clearly demonstrated, with the start of autoignition occurring on the right-hand-side of the bore between the intake and exhaust valve. The swirling motion was in 'clockwise' direction hence the origin of each path of motion can be spotted accordingly. The results in Fig. 6 also confirm quantitatively the absence of large-scale swirling motion of the autoignited front for double-injection strategy. Considering the swirling combustion pattern to be partially an effect of the in-cylinder flow from residual momentum of the hydrogen jets, it was initially conjectured that the phenomenon could become stronger with longer injection-pulse width, *i.e.* with
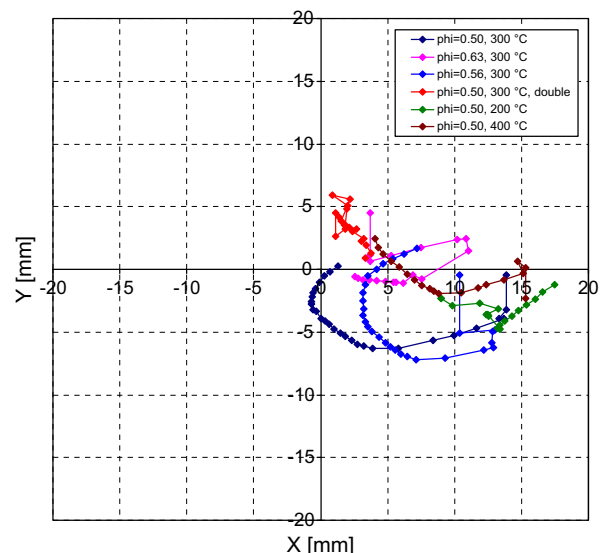

Fig. 6. Locations of flame centroids of area.

increased equivalence ratio under single-injection strategy. However, it was found that the centroids of leaner flames generally displaced a wider span during the advancement of reactions (*e.g.*, ϕ = 0.50 in Fig. 6), *i.e.* gradual decrease of hydrogen percentage in the mixture by shorter pulses of single injection led to stronger flame swirling pattern. This suggested that, whilst the start of autoignition was likely to happen at a specific in-cylinder spot dictated primarily by fuel concentration and temperature fields, progression of the autoignited front was dominated by the coupling between the in-cylinder flow imposed by the injection event and the fuel concentration field. More specifically, it can be said that richer flames were not as prone to following the in-cylinder swirling flow as closely as leaner flames (with weaker rates of heat release) did, or that leaner mixtures were locally 'too lean' in the middle of the bore due to stratification effects discussed earlier, preventing rapid flame expansion towards that area. Measurements of unburned hydrogen in the exhaust pipe may shed some more light on this issue.

Figures 7 and 8 show speeds of flame motion derived by using the location of centroids and their displacement in time. For this characterisation, it was considered informative to employ different measures of flame centroid speed. A 'global' centroid speed was calculated by measuring the distance of the flame's centroid from the centre of the cylinder's bore at any crank angle and dividing

it by the time it had taken for that centroid to be at that point in space at that crank angle after the first site of autoignition. As such it represented a flame centroid speed biased more towards 'bulk' motion and essentially filtered the effects of local smaller-scale motion. Additionally, by calculating the change in flame centroid displacement in time along the path of the flame's centroid motion, *i.e.* using a local 'finite-difference' approach between flame centroids from one crank angle to the next, a 'local' flame centroid speed was also obtained; this allowed for effects of smaller scales on the flame's centroid motion to be included. In Fig. 7 the global flame centroid displacement speed for ϕ = 0.50 shows initial values in excess of 40 m/s for 300 °C and 400 °C, decreasing gradually to levels of the order 10 m/s after 15° CA from the start of autoignition. For 200 °C, the corresponding values were of the order 20–25 m/s, dropping down to levels of ~7 m/s close to the end of combustion. The split injection strategy at 300 °C exhibited much slower 'global' flame centroid displacement speeds from the centre of the bore, with initial vales of ~13 m/s that rapidly decreased to levels of 7 m/s or lower after just 5° CA (and remained fairly steady after that till combustion completion). The flame centroid was displaced 'locally' with speeds of the order 12 m/s at the early stages of combustion with 300 °C and 400 °C intake temperature and quickly stabilised to levels of ~3–5 m/s after the first 10° CA of combustion. The 'local' flame centroid displacement with 200 °C intake temperature was broadly similar, with initial values as high as ~10 m/s, dropping quickly to levels as low as 1 m/s after the first 10° CA of combustion, only to increase gradually again to levels slightly in excess of 5 m/s about 5° CA later. The split injection strategy demonstrated levels of 'local' flame centroid displacement speed much closer to the 'global' equivalent measure, with values of up to 10 m/s within the first 10° CA, decreasing to 1–2 m/s towards combustion completion as the non-swirling flame 'aligned' gradually itself with the centre of the bore. In Fig. 8, for fixed intake temperature of 300 °C, the richer mixture with ϕ = 0.63 demonstrated quite high initial values of centroid displacement speed even on a 'local' scale, in excess of 20 m/s. The mixture with ϕ = 0.56 exhibited displacement speeds of similar level on 'local' and 'global' scale with values in the range 10–15 m/s.

3.2.3. Flame expansion

The flame images were also processed to derive a measure of flame 'expansion' or 'growth' speed. This was done by using the enflamed area at each crank angle to derive the radius of an equivalent circle with the same area to that measured; then a growth speed was derived as a 'finite difference' from one crank angle to the next (*i.e.* per time step of imaging). This methodology was selected because it has been used in the past for the calculation of flame expansion speeds in SI engines with various fuels and hence can provide grounds for relative comparisons.

Figures 9 and 10 show the flame growth speeds in relation to time after the start of autoignition. It can be observed that the flame's expansion speed exhibited initial values in the range 15–30 m/s; those values were derived by extrapolation to 'zero' enflamed area earlier than the first site of autoignition (*i.e.* earlier than 1° CA in those graphs), hence they need to be used with a degree of caution as far as their absolute magnitudes are concerned; however, they are still useful for comparative purposes between the different conditions of ϕ and intake temperature. The speeds obtained after the initial expansion phase, *i.e.* at ~5° CA after the start of combustion, were ~5 m/s for most conditions. This value was broadly maintained up to ~10° CA after the start of combustion for ϕ = 0.63 with 300 °C intake temperature, but decreased quickly to levels of 2 m/s for the other mixtures and temperatures within the same timescale. The double-injection strategy with ϕ = 0.50 and 300 °C demonstrated a lower initial value of flame expansion, 15–20 m/s, but maintained values close to ~5 m/s for
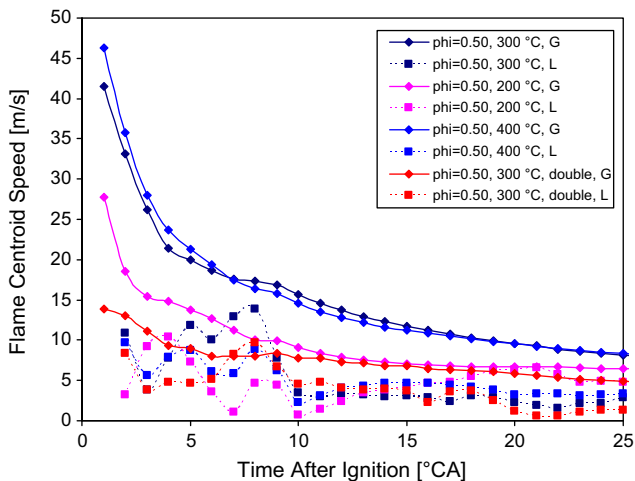

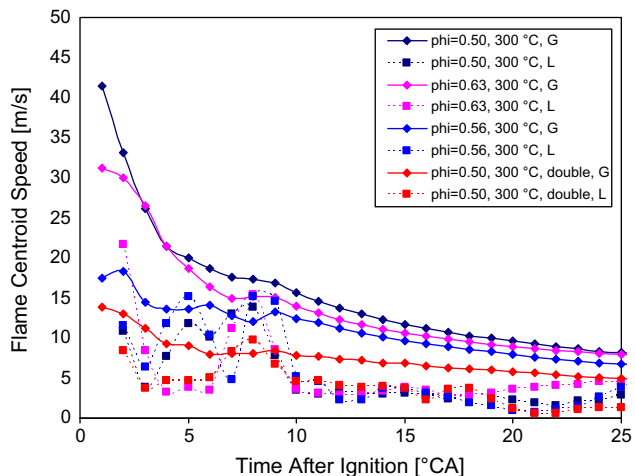**Fig. 7.** Flame centroid speed, effect of intake temperature.

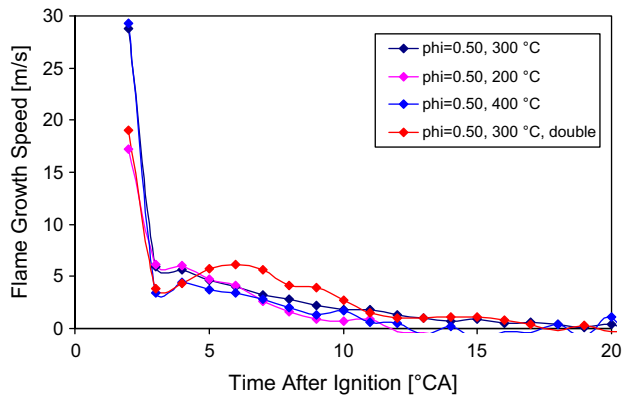**Fig. 8.** Flame centroid speed, effect of equivalence ratio.

Fig. 9. Flame growth speed, effect of equivalence ratio.
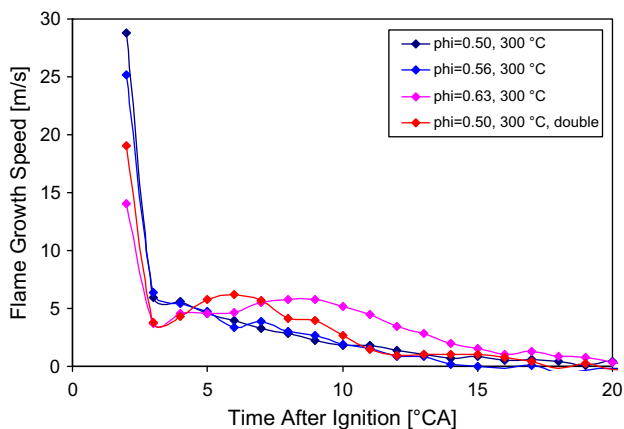

Fig. 10. Flame growth speed, effect of intake temperature.

longer than the single-injection at the same conditions (typically from 5–10° CA). It may be said that the single-injection strategy, following much higher flame expansion speeds initially (∼30 m/s), it had probably 'exhausted' its potential for further fast expansion and decreased gradually to 'zero' levels after 15° CA from the timing of the first site of autoignition.

Analysis was also carried out to compare those speeds with typical flame expansion speeds of SI hydrogen combustion in the same engine. Hydrogen SI flames at 1000 RPM for ϕ = 0.50–0.83 have shown flame growth rates in the range of about 10–40 m/s (depending on injection strategy, DI or PFI); these were at lower engine load (0.5 bar intake pressure) and with lower amount of residual gas trapping due to different valve timings [38]. Therefore, the rate of hydrogen's autoignition and progression was comparable to, but lower than, the expansion speeds of SI hydrogen flames at similar values of equivalence ratio.

To analyse this further, differences in flame expansion speed at the in-cylinder conditions of SI and HCCI were considered using the limited data in the literature on hydrogen's burning velocities at engine-like conditions [44–46]. For SI operation with spark advance of 15° CA in [38], the in-cylinder pressure at ignition timing was about 7–8 bar (depending on injection strategy – DI or PFI), similar in range to that at the crank angle of hydrogen's start of autoignition under HCCI operation (depending on injection strategy – single or double on this occasion). Therefore, differences in flame expansion speeds due to pressure conditions at the time of ignition could be considered small; even if pressure differences of the order 0.5–1.0 bar existed at the timing of ignition between the two modes of engine operation, the effect on laminar burning

velocity would be quite small in comparison to effects from differences in temperature and residual gas fraction between SI and HCCI combustion modes at the respective timings of their ignition. Temperature at ignition timing was of the order 450 K for SI operation and ∼900 K for controlled autoignition operation, whilst residual gas fraction was 0.22 for SI in comparison to 0.42 for HCCI. Considering that the higher initial temperature under HCCI operation would lead to ∼2.4 times greater nominal laminar burning velocity, and that the lower residual gas fraction would lead to ∼6 times higher nominal laminar burning velocity for SI operation (with some dependence on ϕ), the overall net effect for HCCI conditions would be a laminar burning velocity of ∼40% the laminar burning velocity of the hydrogen SI engine experiments in [38]. This is actually consistent with the values of expansion speed calculated for HCCI in the current work. More specifically, hydrogen flames showed peak expansion speeds of ∼20 m/s for SI operation with DI in [38]; this translates to ∼7.5 m/s at the respective conditions of HCCI if one accounts for the 40% estimation made above. Considering also that burning velocities can be deduced from expansion velocities by dividing the latter by the ratio of densities of the unburned and burned mixtures (that would be for HCCI about half that for SI due to the higher temperature at the timing of ignition from calculations using [47]), the burning velocities for HCCI would match those of SI if SI operation was run at the same conditions of dilution and intake temperature.

Further discussion of this issue based on the current set of data and the limited theoretical analysis of HCCI combustion in the literature is not trivial. Possible modes of autoignition in HCCI engines have been discussed in relation to end gas autoignition in SI engines, e.g., [48], including modelling of hydrogen autoignition at 1000 K and 50 bar with and without presence of hot spots, e.g., [49], and the following five regimes of autoignition have been summarised: (i) thermal explosion, (ii) supersonic autoignitive deflagration, (iii) developing and developed detonation, (iv) subsonic autoignitive deflagration, and (v) laminar burning deflagration at the laminar burning velocity. Specifically, when subsonic or slow deflagrative autoignition is established, at the onset of autoignition the speed of reaction is of the order 300 m/s but rapidly decreases to ∼40 m/s as the autoignition front is left behind the acoustic wave and there is no mutual reinforcing effect between the two. This mode may be considered broadly in agreement with data presented previously on HCCI of hydrocarbons where autoignition rates have been found to occur with values of the order 40–100 m/s in engines with compression ratio in the range 15:1–20:1 and typically with ∼1000 K and ∼50 bar at the timing of autoignition (i.e. similar conditions to those modelled in [48,49]). Subsonic deflagration was found likely to develop in [49] when the radius of the hot spot had been decreased to about 1 mm in size; further decrease in the size of the hot spot, along with an increase in the temperature gradient, resulted in laminar burning deflagration with the speed of the autoignited front falling to values of ∼15 m/s driven by the chemistry and molecular transport processes. Considering that the work of [49] did not consider presence of large amount of residuals, the lower values of flame speeds measured in the current study seem again consistent.

3.3. Oh laser induced fluorescence imaging

3.3.1. Analysis of typical HCCI phenomena on a planar basis

Currently accepted mechanisms of HCCI combustion of hydrocarbon fuels assume that no flame propagation occurs, but a fundamental question still is whether HCCI combustion can be associated locally with flame propagation. An interesting thought has always been whether it is possible that HCCI has 'normal' flame propagation but with a large number of ignition kernels in contrast to the single kernel created by the spark plug in SI engines. For

example, Kaizer et al. [50] obtained detailed exhaust emissions data from a single-cylinder direct injection HCCI engine operating on gasoline fuel. For $\phi > 1.5$, CO was the primary carbon oxide, while for $\phi < 0.2$, CO_2 was the major carbon oxide. This suggested that for $\phi < 0.2$ flame propagation may occur between multiple autoignition sites and adiabatic compression calculations indicated that for $\phi < 0.2$ the compression temperature was sufficiently high to support flame propagation between ignition sites over short distances.

To study this issue *in situ*, LIF images of acetone-doped heptane HCCI have been published by some researchers. For example, Hultqvist et al. [51] used high-speed LIF and indicated that there was no real propagating flame with HCCI as with SI. Regions of fuel consumption gradually appeared to grow darker and darker rather than propagating. This suggested that reactions were taking place everywhere simultaneously but at different rates due to local inhomogeneities in temperature or fuel concentration. However, later in the combustion phase, sharp fuel-concentration gradients could be found in some regions, and the fuel distribution in those regions was similar in appearance to the distribution associated with flames in SI engines. Subsequent similar work by Hultqvist et al. [52] led to estimating a global flame expansion speed of 82 m/s. However, evaluation of small-island growth showed that the combustion zone expanded sometimes locally with a speed as low as 15 m/s. This speed is close to the flame propagation speed that has been found in SI engines, *e.g.*, [42,43]. Work by Richter et al. [53] with acetone LIF and OH LIF demonstrated that in-cylinder maps of OH LIF with heptane/*iso*-octane blends were very inhomogeneous, irrespective of mixing preparation strategy. This was considered a result from even small variations in residual gas concentration or temperature that could be sufficient to generate the local combustion kernels. Further studies of simultaneous OH and formaldehyde LIF have decoupled the early slow oxidation mechanism from and the later faster combustion [35–37].

3.3.2. Analysis of hydrogen HCCI on a planar basis

Clearly none of the phenomena linked to the production or consumption of carbon-based species is expected when studying hydrogen flames (especially in an unlubricated optical engine), but analysis of autoignition data from HCCI engines fuelled by hydrocarbons was considered useful in comparing existing HCCI insights with observations made in this paper. As a baseline comment, it needs to be said that HCCI of heptane in the engine of the current study has been characterised by flame chemiluminescence imaging and has been found to behave similarly to data published by previous researchers on the subject and no attempt was made to study this mechanism further.

However, considering the similarity between the speeds of flame expansion for hydrogen HCCI and SI operation discussed in the previous section, it was deemed essential to look into the planar structure of the flame after the onset of autoignition. Chemiluminescence imaging is a line of sight technique usually unable to detect underlying structures, hence if local autoignition kernels existed (in which chemical reactions started ahead or within the main combustion area), they could have been masked by the line of sight integration. Therefore, OH LIF was selected in order to shed more light on the in-cylinder hydrogen autoignition mechanism on a planar frame of analysis that would eliminate ambiguities related to line-of-sight imaging integration.

Figure 11 illustrates OH LIF images of hydrogen HCCI flames for different values of equivalence ratio in the range $\phi = 0.40$–0.59 and with intake temperature of 300 °C. For each value of equivalence ratio those demonstrate the OH development throughout the first 10° CA after the onset of autoignition in steps of 2° CA; images are from different cycles and demonstrate the degree of cyclic variability in the flame's 2D 'sliced' structure. There is a consistent trend

with observations made during the high-speed imaging study; autoignition was found to start from the right-hand-side of the combustion chamber and to develop gradually towards the other side of cylinder. Cyclic variability in the shapes of those flames was more evident than in the chemiluminescence images. Specifically, the first four images in the first column of Fig. 11 show a typical pattern of OH development for $\phi = 0.59$ over the first 10° CA from the timing of the first site of autoignition (those images come from different cycles as the study was not crank-angle resolved within the same cycle). The last two images in that column show images of OH LIF from two different cycles that exhibited large-scale distortion. Decreasing the equivalence ratio from $\phi = 0.59$ to $\phi = 0.50$ did not lead to substantially different development of the autoignition patterns on a planar frame (second column in Fig. 11). However, leaner mixtures appeared to have stronger tendency to develop fragmentation in the recorded OH patterns, as well as a more wrinkled and distorted front, with greater variability on a cycle-by-cycle basis than the chemiluminescence images indicated; the reader is encouraged to compare gradually the columns from left to right in Fig. 11 as the equivalence ratio is decreased from $\phi = 0.59$ to $\phi = 0.40$. In particular, the third column of Fig 11 illustrates some highly distorted OH patterns for $\phi = 0.50$ for comparison with the typical less distorted OH patterns of the second column at the same equivalence ratio. Finally, the fourth column demonstrates the cyclic variability in OH LIF images for $\phi = 0.40$ where fragmentation was common.

The effect of intake air temperature on the in-cylinder OH patterns showed that higher intake temperatures resulted to a larger part of the optical bore lit by OH distribution than at lower temperatures at the same crank angle before TDC, whereas the overall rate of autoignition on average did not appear to vary substantially over the temperature range of 200–400 °C tested; this was in agreement with the pressure history and chemiluminescence results discussed earlier, hence images at different temperatures have not been included in Fig. 11. Nevertheless, it may be useful to note that temperature had an effect on the edges of the OH maps; lower intake air temperature led to less defined OH contours and hotter intake air led to a more 'structured' front with sharper flame contour. Compression of unburned regions by the expanding hot product gases is believed to lead to a sharpening of structures [51].

Overall, the OH LIF imaging study strengthened the notion suggested by chemiluminescence imaging, *i.e.* once hydrogen autoignition had initiated, it appeared to develop gradually in 'propagation-like' fashion rather than in the typical HCCI pattern of fast combustion with multiple autoignition kernels seen for hydrocarbon-based fuels. The octane number hydrogen may have played a critical role in determining this characteristic flame pattern at the studied conditions. Autoignition appeared to start mainly from one initial spot, presumably due to locally favourable fuel concentration and temperature fields and then developed into a combustion front similar to that of a deflagration flame, as if the fuel's resistance to autoignition in conjunction with the degree of stratification in the rest of the cylinder prevented the combustion to proceed in the traditional manner of HCCI development recorded for hydrocarbons. Moreover, at an early stage of the current work, when various injection strategies were under investigation, it was found that earlier injections led to advanced start of autoignition and it was conjectured that a diffusion-like mechanism of autoignition might have been taking place. However, after comparing OH LIF patterns of hydrogen HCCI with those yielded by diffusion flames of hydrocarbons (*e.g.*, [54]), it was clear that the OH distribution did not exhibit a hollow structure as such where the fuel rich premixed oxidation would take place in Diesel-like operation. This may act to strengthen further the hypothesis of autoignited hydrogen flames burning at certain conditions similarly to spark-ignited flame fronts.
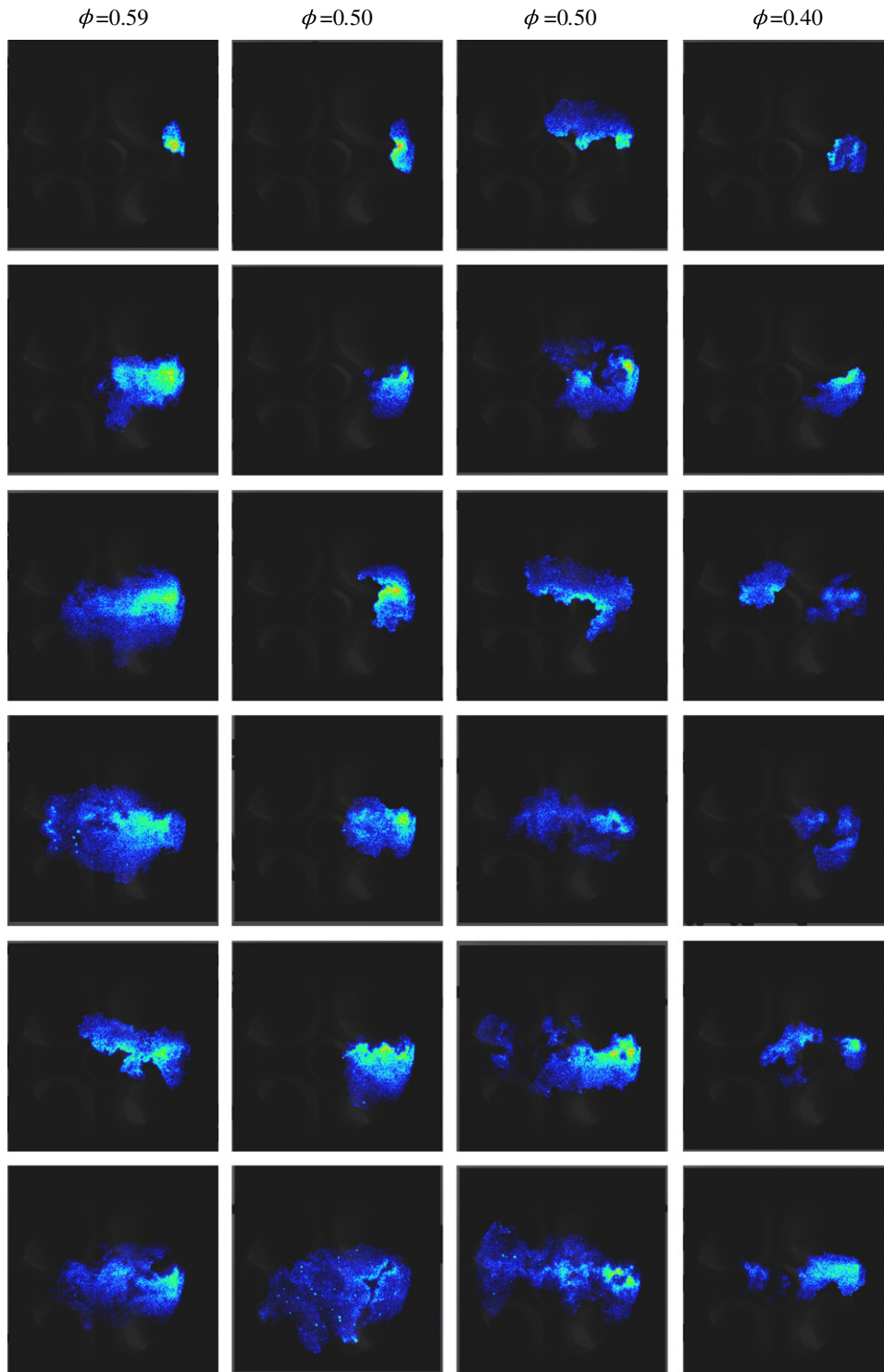
$\phi=0.59$ $\phi=0.50$ $\phi=0.50$ $\phi=0.40$

Fig. 11. OH LIF images: ϕ = 0.40–0.59, 300 °C (intake valves at the top, exhaust valves at the bottom).

Finally, the nature of coupling spark ignition to controlled autoignition was also looked into with OH LIF. Despite the fact that 'knocking' hydrogen combustion has been studied in the literature (primarily in thermal engines), there are still questions on its nature and how hydrogen exhibits a marked tendency to knock. Figure 12 shows OH LIF images of spark-initiated hydrogen combustion at ϕ = 0.50 with intake air temperature of 120 °C; at this temperature hydrogen HCCI operation could not be initiated and sustained on its own. The images in Fig. 12 correspond to 5° CA after spark tim-

ing; they are from different cycles and illustrate the degree of cyclic variability. It was consistently clear on a cycle-by-cycle basis that after the onset of spark the flame developed initially quite symmetrically from the spark plug to the cylinder walls; small-scale wrinkling was discernible on the OH boundaries, similar in nature to observations made by OH LIF images of typical hydrogen SI combustion in the same engine without air preheating in [38]. As the spark-ignited flame front advanced past about 4–5° CA after the spark onset, autoignition occurred ahead of the spark-ignited
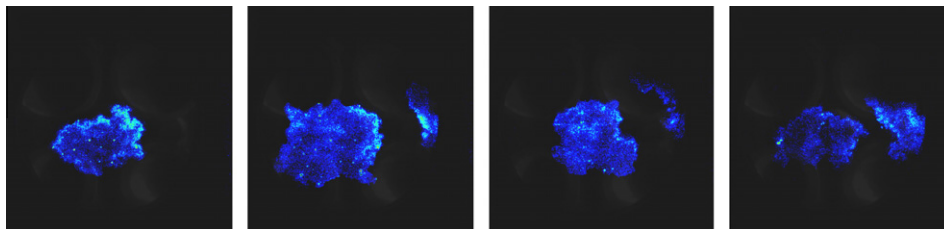
Fig. 12. OH LIF images: ϕ = 0.50 with SI (intake valves at the top, exhaust valves at the bottom).

flame. This appeared again on the right-hand-side of the combustion chamber at the same location where autoignition occurred for HCCI operation. A second flame front was established from that autoignition site, as clearly shown in the rest of the images of Fig. 12 from three different engine cycles. The two flame fronts expanded towards each other at similar rates and in similar fashion to what has been observed in twin-spark engines; they eventually met reaching completeness of combustion. Therefore, it may be said that, depending on operating conditions, end-gas hydrogen ignition does not necessarily involve knocking combustion of the same nature to that of hydrocarbon fuels. For comparison with a study of heavier knocking in a hydrogen-fuelled optical SI engine of different type and running conditions the interested reader is guided to the work of [55].

4. Summary and conclusions

The current paper presented results from an optical study of controlled autoignition of hydrogen in a pentroof-type engine originally designed for SI operation with liquid fuels. The engine speed was fixed to 1000 RPM with the throttle set to wide-open position. Hydrogen fuelling was supplied by direct injection at 100 bar and with equivalence ratio in the range ϕ = 0.40–0.63. Controlled autoignition was achieved by inlet air preheating in the range 200–400 °C and residual gas recirculated internally by negative valve overlap. Crank-angle resolved flame chemiluminescence images were acquired for a series of consecutive cycles in order to calculate in-cylinder rates of flame expansion and motion. Single and double (*i.e.* 'split' per cycle) hydrogen injection strategies were employed in order to identify the effect of mixture preparation on autoignition's timing and spatial development. Analysis was also carried out by planar LIF of OH that recorded more detailed features of the autoignition pattern and its development. An attempt was also made to review relevant in-cylinder phenomena from the limited literature on hydrogen-fuelled optical DISI engines and make comparisons where appropriate with DI HCCI to aid interpretation of the results. The conclusions of this study can be summarised as follows:

- The change in intake air temperature by 200 °C from 200–400 °C had a small influence on the timing of the first sign of flame chemiluminescence in the images (~3° CA) and the onset of heat release on the pressure traces.
- The nature of hydrogen's autoignition was very different to typical HCCI phenomena observed with hydrocarbon fuels. For ϕ = 0.50 autoignition started between the intake and exhaust valves close to the wall (on the right-hand-side of the combustion chamber) and followed a clockwise swirling pattern during development.
- For ϕ = 0.63 autoignition started between the intake and exhaust valves, again on the right-hand-side of the combustion chamber, but not in close proximity to the cylinder's walls. Initial expansion was generally of 'circular' shape but once the

flame size had reached about half that of the optical bore it expanded towards the left-hand-side area of the chamber and it started to exhibit large-scale distortion akin to the swirling observed for ϕ = 0.5.
- The location of the start of autoignition had limited spatial variability on a cycle-by-cycle basis. Following autoignition, combustion progressed with broadly the same pattern of development on a cycle-by-cycle basis too. The cycle-to-cycle variability in the timing of autoignition was also quite small, typically in the range ±2° CA.
- Cross-analysis of mixture formation and PIV data from the literature indicated that the swirling motion of autoignition might be a result of momentum exchange between the hydrogen DI jets and the in-cylinder air, as well as strong fuel stratification (with most fuel concentrated close to the walls and very lean areas in the middle).
- Autoignition with double-injection strategy for ϕ = 0.50 and 300 °C exhibited no swirling pattern; combustion started ~10–12° CA earlier than with single injection, close to the centre of the bore, and developed symmetrically towards the walls. This could be explained by a weaker effect of the two short injection pulses on the air flow and by better mixing that led to lower stratification (hence to absence of very lean areas in the middle of the bore).
- A measure of flame-centroid displacement speed from the centre of the bore, termed 'global', showed that for ϕ = 0.50 combustion's motion was initially associated with values in excess of 40 m/s for 300 °C and 400 °C, decreasing gradually to levels of the order 10 m/s after 15° CA from the start of autoignition. For 200 °C, the respective values were ~20–25 m/s and ~7 m/s.
- For ϕ = 0.50 with 300 °C and 400 °C the flame centroid was displaced along the path of motion, *i.e.* 'locally', with speeds of ~12 m/s at the early stages of combustion, and stabilised to levels of ~3–5 m/s after the first 10° CA of combustion. For 200 °C, initial values were ~10 m/s, dropping to levels as low as 1 m/s after the first 10° CA.
- The charge with ϕ = 0.63 demonstrated quite high initial values of flame-centroid displacement speed even on a 'local' scale, in excess of 20 m/s. For ϕ = 0.56 displacement speeds were of similar level on 'local' and 'global' scale, with values in the range 10–15 m/s.
- The double-injection strategy exhibited slower 'global' flame centroid displacement speeds than single injection, with initial vales of ~13 m/s that decreased to levels of ~7 m/s or lower after just 5° CA. The 'local' flame centroid displacement speed was close to the 'global' equivalent measure, with values of up to 10 m/s within the first 10° CA, decreasing to 1–2 m/s towards combustion completion.
- A measure of flame expansion speed exhibited initial values in the range 15–30 m/s. The speeds obtained at ~5° CA after the start of combustion were ~5 m/s for most conditions. This value was broadly maintained up to ~10° CA after the start of combustion for ϕ = 0.63 with 300 °C intake temperature but

decreased quickly to levels of 2 m/s for the other mixtures and temperatures within the same timescale.

- The double-injection strategy demonstrated a lower initial value of flame expansion, 15–20 m/s but maintained values close to ~5 m/s for longer than the single-injection at the same conditions (typically from 5–10° CA).
- Overall the acquired data pointed to subsonic slow deflagrative autoignition at the conditions studied. Cross-analysis with data from SI operation indicated that the burning velocities for HCCI would match those of SI if SI was run at the same conditions of dilution and intake temperature.
- OH LIF in the range revealed that leaner mixtures had stronger tendency to exhibit fragmentation in the combustion pattern, as well as a more wrinkled and distorted front, with greater cyclic variability than chemiluminescence images indicated. It also strengthened the hypothesis suggested by chemiluminescence, i.e. once hydrogen autoignition had initiated, it developed more in 'propagation-like' fashion rather than in the typical HCCI pattern of fast combustion with multiple autoignition kernels seen for hydrocarbon fuels.
- Coupling SI to HCCI showed that when the spark-ignited flame front grew past ~5° CA after spark timing, autoignition occurred ahead of the flame at the same location where autoignition occurred for HCCI. A second flame front was established from the autoignition site and the two flame fronts expanded at similar rates in similar fashion to what has been observed in twin-spark engines. Therefore, end-gas hydrogen ignition with SI operation does not necessarily involve knocking combustion of the same nature to that of hydrocarbon fuels.

Running the engine with fully premixed charge could provide decoupling of the combustion development pattern from closed-valve DI effects and allow further analysis. However, considering the high intake temperatures required and the simultaneous need to achieve stable operation without intake autoignition/backfiring problems, use of multiple injections per cycle (i.e. greater than two used here) could act as a strategy to 'homogenise' the mixture better in future work. In that respect, comparisons would be beneficial with simultaneous OH LIF and PIV, along with numerical simulation of mixture formation and temperature distribution using real-gas thermodynamics. Quantitative analysis of the degree of wrinkling and large-scale distortion of the OH patterns for HCCI and SI based on methods in [56] will provide further insights. Measurements of unburned hydrogen and NO$_X$ in the exhaust would also add to our understanding.

Acknowledgments

References

[1] J.M. Norbeck, J. Heffel, T. Durbin, M. Montano, B. Tabbara, J. Bowden, Hydrogen Fuel for Surface Transportation, SAE, Warrendale, PA, USA, 1996.
[2] C.M. White, R.R. Steeper, A.E. Lutz, Int. J. Hydrogen Energy 31 (2006) 1292–1305.
[3] S. Verhelst, R. Sierens, S. Verstraeten, A Critical Review of Experimental Research on Hydrogen Fueled SI Engines, SAE Paper 2006-01-0430, 2006.
[4] S. Verhelst, S. Verstraeten, R. Sierens, Proc. IMechE, Part D, J. Automobile Eng. 221 (2007) 911–920.
[5] S. Verhelst, T. Wallner, Prog. Energy Combust. Sci. 35 (2009) 490–527.
[6] L.M. Das, Int. J. Hydrogen Energy 21 (1996) 789–800.
[7] G.A. Karim, Int. J. Hydrogen Energy 28 (2003) 569–577.
[8] R.F. Cracknell, J.L. Alcock, J.J. Rowson, L.C. Shirvill, A. Üngüt, Safety Considerations in Retailing Hydrogen, SAE Paper 2002-01-1928, 2002.
[9] H. Li, G.A. Karim, An Experimental Investigation of SI Engine Operation on Gaseous Fuels Lean Mixtures, SAE Paper 2005-01-3765, 2005.
[10] J.W. Heffel, Int. J. Hydrogen Energy 28 (2003) 901–908.
[11] J.W. Heffel, Int. J. Hydrogen Energy 28 (2003) 1285–1292.
[12] S. Verhelst, J. De Landtsheere, F. De Smet, C. Billiouw, A. Trenson, R. Sierens, Effects of Supercharging, EGR and Variable Valve Timing on Power and Emissions of Hydrogen Internal Combustion Engines, SAE Paper 2008-01-1033, 2008.
[13] A.M. Nande, S. Szwaja, J.D. Naber, Impact of EGR on Combustion Processes in a Hydrogen Fuelled SI Engine, SAE Paper 2008-01-1039, 2008.
[14] J.G. Ingersoll, Natural Gas Vehicles, Fairmont Press, 1996.
[15] A. Welch, D. Mumford, S. Munshi, J. Holbery, B. Boyer, Challenges in Developing Hydrogen Direct Injection Technology for Internal Combustion Engines, SAE 2008-01-2379, 2008.
[16] S. Verhelst, R. Sierens, Combustion Studies for PFI Hydrogen IC Engines, SAE Paper 2007-01-3610, 2007.
[17] T. Wallner, H. Lohse-Busch, Performance, Efficiency and Emissions Evaluation of a Supercharged, Hydrogen-Powered, 4-Cylinder Engine, SAE Paper 2007-01-0016, 2007.
[18] T. Blotevogel, J. Egermann, J. Goldlücke, A. Leipertz, M. Hartmann, M. Schenk, M. Berckmüller, Developing Planar Laser-Induced Fluorescence for the Investigation of the Mixture Formation Process in Hydrogen Engines, SAE Paper, 2004-01-1408.
[19] W. Kirchweger, R. Haslacher, Exp. Fluids 43 (2007) 329–340.
[20] C.M. White, A Qualitative Evaluation of Mixture Formation in a Direct-Injection Hydrogen-Fuelled Engine, SAE Paper 2007-01-1467, 2007.
[21] C.M. White, Int. J. Engine Res. 8 (2007) 185–204.
[22] V.M. Salazar, S.A. Kaiser, An Optical Study of Mixture Preparation in a Hydrogen-Fuelled Engine with Direct Injection Using Different Nozzle Designs, SAE Paper 2009-01-2682, 2009.
[23] V.M. Salazar, S.A. Kaiser, Influence of the In-Cylinder Flow Field (Tumble) on the Fuel Distribution in a DI Hydrogen Engine Using a Single-Hole Injector, SAE Paper 2010-01-0579, 2010.
[24] S. Kaiser, C.M. White, PIV and PLIF to Evaluate Mixture Formation in a Direct-Injection Hydrogen-Fuelled Engine, SAE Paper 2008-01-1034, 2008.
[25] T. Tsurushima, A. Harada, Y. Iwashiro, Y. Enomoto, Y. Asaumi, Y. Aoyagi, Thermodynamic Characteristics of Premixed Compression Ignition Combustions, SAE Paper 2001-01-1891, 2001.
[26] P.G. Aleiferis, A.G. Charalambides, Y. Hardalupas, A.M.K.P. Taylor, Y. Urata, Modelling and Experiments of HCCI Engine Combustion with Charge Stratification and Internal EGR, SAE Paper 2005-01-3725, 2005.
[27] P.G. Aleiferis, A.G. Charalambides, Y. Hardalupas, A.M.K.P. Taylor, Y. Urata, Autoignition Initiation and Development of n-Heptane HCCI Combustion Assisted by Inlet Air Heating, Internal EGR or Spark Discharge: An Optical Investigation, SAE Paper 2006-01-3273, 2006.
[28] P.G. Aleiferis, A.G. Charalambides, Y. Hardalupas, A.M.K.P. Taylor, Y. Urata, Int. J. Veh. Des. 44 (2007) 41–61.
[29] P.G. Aleiferis, A.G. Charalambides, Y. Hardalupas, A.M.K.P. Taylor, Y. Urata, Proc. IMechE, Part D, J. Automobile Eng. (2008) 2171–2183.
[30] M. Christensen, A. Hultqvist, B. Johansson, Demonstrating the Multi-Fuel Capability of a Homogeneous Charge Compression Ignition Engine with Variable Compression Ratio, SAE 1999-01-3679, 1999.
[31] M. Amann, T.W. Ryan III, N. Kono, HCCI Fuels Evaluations – Gasoline and Diesel Boiling Ranges, SAE Paper 2005-01-3727, 2005.
[32] O. Stenlåås, M. Christensen, R. Egnell, B. Johansson, F. Mauss, Hydrogen as Homogeneous Charge Compression Ignition Engine Fuel, Paper 2004-01-1976, 2004.
[33] J.M. Gomes Antunes, R. Mikalsen, A.P. Roskilly, Int. J. Hydrogen Energy 33 (2008) 5823–5828.
[34] P.A. Caton, J.T. Pruitt, Int. J. Engine Res. 10 (2009) 45–63.
[35] N. Graf, J. Gronki, C. Schulz, T. Baritaud, J. Cherel, P. Duret, J. Lavy, In-Cylinder Combustion Visualization in an Auto-Igniting Gasoline Engine using Fuel Tracer- and Formaldehyde-LIF Imaging, SAE Paper 2001-01-1924, 2001.
[36] Z. Peng, H. Zhao, N. Ladommatos, Proc. IMechE, Part D, J. Automobile Eng. 217 (2003) 1125–1134.
[37] R. Collin, J. Nygren, M. Richter, M. Aldén, L. Hildingsson, B. Johansson, Simultaneous OH and Formaldehyde LIF Measurements in an HCCI Engine, SAE Paper 2003-01-3218, 2003.
[38] P.G. Aleiferis, M.F. Rosati, Flame Chemiluminescence and OH LIF Imaging in a Hydrogen-Fuelled Spark-Ignition Engine, International Journal of Hydrogen Energy, 37 (2012) 1797–1812.
[39] M.F. Rosati, P.G. Aleiferis, Hydrogen SI and HCCI Combustion in a Direct-Injection Optical Engine, SAE International Journal of Engines, vol. 2, SAE Paper 2009-01-1921, 2009, pp. 1710–1736.
[40] Lotus Engine Simulation Software, <http://www.lesoft.co.uk/index.html>, 2010.
[41] M.F. Brunt, A.L. Emtage, Evaluation of IMEP Routines and Analysis Errors, SAE Paper 960609, 1996.
[42] J. Serras-Pereira, P.G. Aleiferis, D. Richardson, S. Wallace, Mixture Formation and Combustion Variability in a Spray-Guided DISI Engine, Transactions of SAE, Journal of Engines, vol. 116(3), Paper 2007-01-4033, 2007, pp. 1332–1356.
[43] P.G. Aleiferis, J. Serras-Pereira, Z. van Romunde, J. Caine, M. Wirth, Combust. Flame 157 (2010) 735–756.
[44] S. Verhelst, A Study of the Combustion in Hydrogen-Fuelled Internal Combustion Engines, PhD Thesis, Ghent University, 2005.
[45] S. Verhelst, R. Woolley, M. Lawes, R. Sierens, Proc. Combust. Inst. 30 (2005) 209–216.

[46] D. Bradley, M. Lawes, K. Liu, S. Verhelst, R. Woolley, Combust. Flame 149 (2007) 162–172.
[47] C. Morley, GASEQ: A chemical equilibrium program for Windows, <http://www.gaseq.co.uk>, 2005.
[48] C.G.W. Sheppard, S. Tolegano, R. Woolley, On the Nature of Autoignition leading to Knock in HCCI Engines, SAE Paper 2002-01-2831, 2002.
[49] X.J. Gu, D.R. Emerson, D. Bradley, Combust. Flame 133 (2003) 63–74.
[50] E.W. Kaiser, J. Yang, T. Culp, N. Xu, M.M. Maricq, Int. J. Engine Res. 3 (2002) 185–195.
[51] A. Hultqvist, M. Christensen, B. Johansson, M. Richter, J. Nygren, J. Hult, M. Aldén, The HCCI Combustion Process in a Single Cycle – High-Speed Fuel Tracer LIF and Chemiluminescence Imaging, SAE Paper 2002-01-0424, 2002.
[52] J. Hult, M. Richter, J. Nygren, M. Alden, A. Hultqvist, M. Christensen, B. Johansson, Appl. Opt. 41 (2002) 2002–2014.
[53] M. Richter, J. Engström, A. Franke, M. Aldén, A. Hultqvist, B. Johansson, The Influence of Charge Inhomogeneity on the HCCI Combustion Process, SAE Paper 2000-01-2868, 2000.
[54] J.E. Dec, E.B. Coy, OH Radical Imaging in a DI Diesel Engine and the Structure of the Early Diffusion Flame, SAE Paper 96083, 1996.
[55] N. Kawahara, E. Tomita, M.K. Roy, Visualization of Autoignited Kernel and Propagation of Pressure Wave during Knocking Combustion in a Hydrogen Spark-Ignition Engine, SAE Paper 2009-01-1773, 2009.
[56] P.G. Aleiferis, A.M.K.P. Taylor, K. Ishii, Y. Urata, Combust. Flame 136 (2004) 283–302.